IOP Publishing | Institute of Physics and Engineering in Medicine Physics in Medicine & Biology

Phys. Med. Biol. **62** (2017) 7855–7873 https://doi.org/10.1088/1361-6560/aa8841

Lung respiration motion modeling: a sparse motion field presentation method using biplane x-ray images

Dong Chen[1], **Hongzhi Xie**[2,3], **Shuyang Zhang**[2]
and Lixu Gu[1,3]

[1] School of Biomedical Engineering, Shanghai Jiao Tong University, Shanghai, People's Republic of China
[2] Department of Cardiothoracic Surgery, Peking Union Medical College Hospital, Beijing, People's Republic of China

E-mail: xiehongzhi@medmail.com.cn and gulixu@sjtu.edu.cn

Received 24 April 2017, revised 21 July 2017
Accepted for publication 24 August 2017
Published 20 September 2017

Abstract

Respiration-introduced tumor location uncertainty is a challenge in the precise lung biopsy for lung lesions. Current statistical modeling approaches hardly capture the complex local respiratory motion information. In this study, we formulate a statistical respiratory motion model using biplane x-ray images to improve the accuracy of motion field estimation by efficiently preserving local motion details for specific patients. Given CT data sets of 18 healthy subjects at end-expiratory and end-inspiratory breathing phases, the respiratory motion field is constructed based on deformation vector fields which are extracted from these CT data sets, and a lung contour motion repository respiratory is generated dependent on displacements of boundary control points. By varying the sparse weight coefficients of the statistical sparse motion field presentation (SMFP) method, the newly-input motion field is approximately presented by a sparse linear combination of a subset of the motion repository. The SMFP method is employed twice in the coefficient optimization process. Finally, these non-zero coefficients are fine-tuned to maximize the similarity between the projection image of reconstructed volumetric images and the current x-ray image. We performed the proposed method for estimating respiratory motion field on ten subject datasets and compared the result with the PCA method. The maximum average target registration error of the PCA-based and the SMFP-based respiratory motion field estimation are 3.1(2.0) and 2.9(1.6) mm, respectively. The maximum average symmetric surface distance of two methods are 2.5(1.6) and 2.4(1.3) mm, respectively.

---

[3] Authors to whom any correspondence should be addressed.

Keywords: statistical motion model, image reconstruction, sparse motion field presentation, computed tomography (CT), biplane x-ray

(Some figures may appear in colour only in the online journal)

1. Introduction

Tumor-position uncertainty caused by respiratory motion in the thorax introduces difficulties in a wide range of clinical applications (Fuerst *et al* 2015). Therefore, precise knowledge of the entire lung motion during the treatment delivery is necessary for effective transthoracic needle biopsy (Yang *et al* 2015). Respiratory motion estimation algorithms offer a possible solution to solve these problems by constructing the deformation vector fields (DVFs) of respiratory motion.

Registration methods have been commonly used in respiratory organ motion estimation. The goal of image registration methods is to estimate the temporal change in the position of interest and the organ shape by describing the correspondence between different respiratory phases in medical images and to extract the DVFs (Guerrero *et al* 2004, Zhang *et al* 2008). Guerrero *et al* and Ehrhardt *et al* extracted the DVF from 4DCT images acquired during free breathing to simulate lung tumor and lung surface motion by a non-linear registration method (Guerrero *et al* 2004, Ehrhardt *et al* 2007), while the deformation field is generated by optimizing the correlation metrics in voxel- or patch-wise intensity patterns of images, such that the anatomical and material properties are not emphasized. Thus, the purpose of biomechanical methods is to combine the material properties to improve the accuracy of registration. The finite element-based elastic framework has been widely used in registration processes. In order to obtain the patient-specific biomechanical properties, Li *et al* proposed a FEM model based on the inhomogeneous lung and introduced a patient-specific and position-specific respiratory motion estimation (Li *et al* 2013). The boundary conditions of the FEM model, which are used to determine the unknown Young's modulus distribution, were obtained from a varying intensity flow block-marching registration algorithm. Compared with the uniform model, the non-uniform FEM model provided a significantly increased precision in lung respiratory motion estimation. However, each patient had to be scanned at least twice to construct the individual patient's respiratory motion model, which led to extra radio dose and potential expense for patients.

Instead of trying to directly estimate the respiratory deformation field for a specific patient, the statistical motion model can be constructed or derived from some medical image, such as x-ray projection images and MRI images. What's more, the statistical motion model has been successfully employed for predicting and tracking motion of the liver, the heart and the lungs (McClelland *et al* 2013). For example, Ehrhardt *et al* presented a statistical 4D mean motion model to estimate lung respiratory motion (Ehrhardt *et al* 2011). The nonlinear intensity-based registration method was employed to extract the DVFs of 17 patients. An average shape and intensity atlas of the lung was then generated from the reference phase images and used as an anatomical reference frame. Finally, the extracted patient-specific DVFs and the anatomical reference frame were used to generate the statistical motion model based on the assumption that breathing dynamics work similarly for all patients. However, this assumption is unrealistic as the result of the respiratory motion field caused by different breathing patterns should be different. In addition, when the local respiratory motion information is only contained in the minority of the samples, it will be ignored in the mean motion modeling approach. For the PCA-based statistical model, the

DVF relative to a reference image is approximated by a linear combination of the mean DVF and a few eigenvectors corresponding to their PCA coefficients. By varying these eigenvectors and coefficients, a new DVF is reconstructed. King *et al* presented a technique for thoracic respiratory motion estimation based on dynamic 3D MRI data and employed a 2D MRI image navigator to drive this PCA-based motion model (King *et al* 2012). In order to evaluate whether or not the current motion model is accurate enough, the 2D MRI image navigator was continuously acquired and provided a feedback to the workflow. A new 3D dynamic MRI data set was acquired to generate a new PCA-based motion model when the current model was not applicable. However, the 2D MRI image-driven motion model is not always feasible in clinical practice due to the high cost to continuously acquire 2D MRI images (Preiswerk *et al* 2014). Thus, a new volumetric image was reconstructed from a reference volumetric image by optimizing the PCA coefficients such that the projection of the new volumetric image matched with an x-ray image, as presented in Li *et al* (2011). By applying the inverted DVF on the reference image, the location of the tumor and the entire lung motion can be achieved. The smallest average 3D error was achieved by using two PCA coefficients. The PCA-based motion model may lead to the loss of local motion details since some PCA eigenvectors, which are statistically insignificant but contained important local motion details, were discarded. Therefore, it is necessary that the statistical respiratory motion model should preserve as much local motion detail as possible for each specific patient. In addition, it is noticed that the respiration motion information contained in a single x-ray image is overlap which also introduced the motion detail loss.

In order to get a better respiratory estimation result, we employ the biplane x-ray images along two orientations to estimate the lung respiratory motion. Biplane x-ray images have been widely used in recent years. Peltz *et al* assessed measures of joint morphology and their relationship with *in vivo* joint motion through biplane x-ray images (Peltz *et al* 2015). Weichert *et al* used the information obtained from biplane x-ray images to align the intravascular ultrasound sequences simultaneously and a 3D volume model of the vessel in the aligned intravascular ultrasound sequences were detected by an active contour algorithm (Weichert *et al* 2004). The generated 3D model was used to improve the accuracy of the inter-vascular brachytherapy treatment planning.

The primary goal of this work is to address the aforementioned challenges by presenting a novel sparse motion field presentation (SMFP) method to construct a statistical respiratory motion model based on biplane x-ray images acquired from orthogonal projections of the lung, such as the Antero–posterior (AP) direction and Left–right (LR) directions. The SMFP-based motion model can be approximately reconstructed by optimizing the weight coefficients for each sample in the respiratory motion repository such that the projection image of a sparse linear combination of a subsample will best match to the x-ray image in each direction. The SMFP method with the x-ray image in the LR direction is employed to isolate a subsample from the whole respiratory motion repository dependent on the lung outline motion of each sample. The purpose is to decrease the sample size to reduce the influence of the uncorrelated breathing pattern and to preserve the lung respiratory motion along the AP direction. Then, the SMFP method will be employed a second time to update the model with the x-ray image along the AP direction. To generate an accurate statistical motion model, the weight coefficients of the subsample are fine-tuned by maximizing the similarity cost between the projection of a new volumetric image and the current x-ray image. The main contribution of this study can be summarized as:

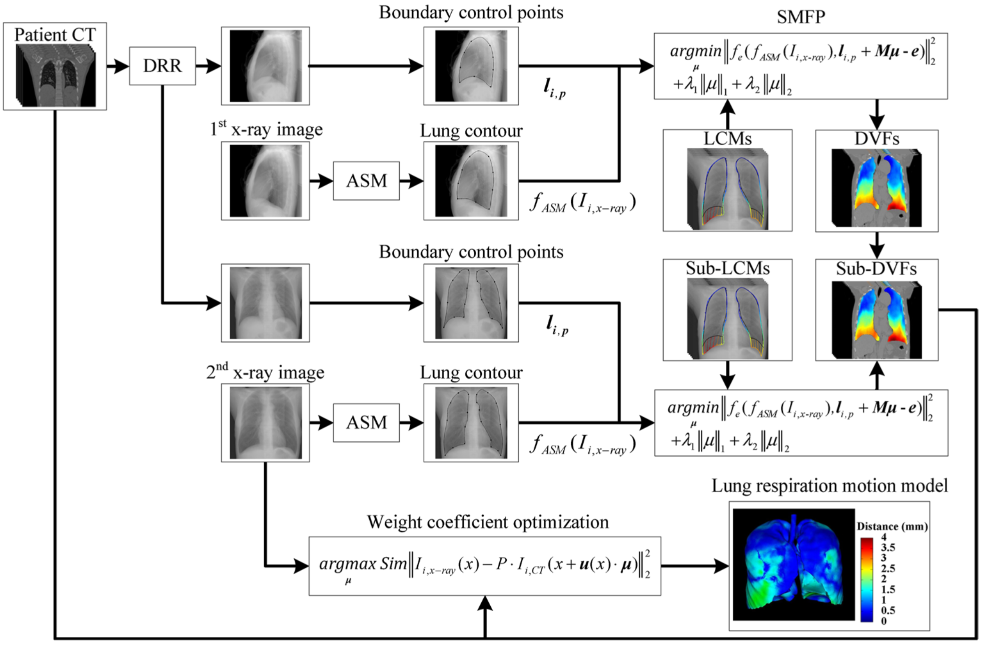

Figure 1. The framework of lung respiratory motion estimation based on two x-ray images along the LR and AP directions.

(1) We propose a novel approach for generating statistical lung motion models which can preserve the location motion details, and estimate the motion of the region of interest (ROI) based on biplane x-ray images along two different orientations. This is the first study that integrates two x-ray images with the statistical respiratory motion model. We also adjust the weight coefficients of the subsample to construct a more precise statistical lung motion model, which can be employed to predict the tumor's location in the biopsy.

(2) We integrate the lung contour motions (LCMs) with the DVFs of the lungs to formulate the SMFP-based model.

2. Method

The novel respiratory motion prior-based estimation framework is shown in figure 1. As shown in the workflow, CT scans ($I_{i,\text{CT}}$) and biplane x-ray images ($I_{i,\text{x-ray}}$) are obtained from the newly-input patient. Therefore, the lung curve ($f_{\text{ASM}}(I_{i,\text{x-ray}})$) and the location ($\boldsymbol{l}_{i,p}$) of the boundary control point in the projection of the CT image are also patient-specific. Moreover, the sparse weight coefficients, obtained based on the SMFP method, will be different which generates a patient-specific DVF for the current patient to describe the motion of the tissue in the lung. In this section, we describe the DVFs acquisition to construct the respiratory DVF repository (section 2.1), the extraction of the lung contour and the reconstruction of the LCM repository from the DVFs (section 2.2). The formation of the SMFP-based respiratory motion model is presented in section 2.3, and finally the optimal adjustment of the sparse weight coefficient is described in section 2.4.

2.1. Patient-specific DVFs acquisition

The respiratory motion repository is constructed from 3D thoracic CT data sets from 18 subjects (see section 3.1 for more details about the image data preparation). Each subject j contains two 3D images $I_{j,\mathrm{EE}}$ and $I_{j,\mathrm{EI}}$ at end-expiratory (EE) and end-inspiratory (EI) phases, respectively. We used a non-parametric discrete method (Heinrich *et al* 2014) to extract the motion field information from $I_{j,\mathrm{EE}}$ to $I_{j,\mathrm{EI}}$. The choice of the registration method we performed in this study is only one possible approach. Other non-linear registration methods that can be used are summarized in Werner *et al* (2014). The registration method aims to find the deformation vector $\boldsymbol{u}$ for each voxel x_i, which minimizes a cost function formulated $F(\boldsymbol{u})$ by patch-based similarity metrics:

$$F\left(\boldsymbol{u}\right)=\sum_{x_i\in\Omega}\left[I_{j,\mathrm{EI}}\left(x_i\right)-I_{j,\mathrm{EE}}(x_i+\boldsymbol{u})\right]^2+\alpha|\nabla\boldsymbol{u}|^2, \tag{1}$$

where Ω represents an image patch for the similarity term, $|\Delta d|$ is the gradient of the displacement vector of each voxel x_i. α is the coefficient of the diffusivity of the regularization.

To build a statistical motion model, the coordinate system from different subjects should be aligned in a common coordinate system. The lung surface of subject 1 was chosen as the reference subject. Then the coordinate system of the specific DVF for each subject is transformed into the reference coordinate frame by computing an affine alignment of the lung surfaces to eliminate the orientation difference. We denote these aligned DVFs by $\boldsymbol{u}(x)=[\boldsymbol{u}_1(x),\boldsymbol{u}_2(x),\ldots\boldsymbol{u}_n(x)]$, where x is the voxel location in CT images, and n is the number of training subjects in the repository.

2.2. Extraction of the LCMs

We apply the aligned entire lung motion field to acquire the contour motion repository, and the lung contour in the projection image of the reference subject at EE breathing phase is determined using the active shape models (ASM) algorithm which presented the lung shape by the boundary control points (Cootes *et al* 1995).

The lung contour is controlled by boundary control points. Therefore, the LCM of each subject can be presented by the motion of these boundary control points. To construct a unified LCM repository, locations of control points in the reference subject are mapped to other subjects in the training data sets. Arbitrarily, subject 1 is chosen as the reference subject. We perform a registration between the projection image $I_{1,p}$ of subject 1 and the projection image $I_{j,p}$ of subject j ($j=2,3,\ldots,n$), where n is the number of training samples. The obtained transformation $\varphi_{j,1}$ is computed as $I_{j,p}=\varphi_{j,1}(I_{1,p})$. Therefore, the corresponding control point location $\boldsymbol{l}_{j,p}$ in the projection image of subject j can be presented as $\boldsymbol{l}_{j,p}=\varphi_{j,1}\left(\boldsymbol{l}_{1,p}\right)$, where $\boldsymbol{l}_{1,p}=\left[l_{1,p,1},l_{1,p,2},\ldots,l_{1,p,k}\right]^T$ is the control point locations in the projection image of the reference subject, and k is the number of boundary control points (see figure 2(a)). Figure 2(b) shows that these boundary control points $\boldsymbol{l}_{1,p}$ in the projection image can determine their locations $\boldsymbol{l}_{1,CT}$ in CT images through the lung model of subject 1. Combined with the aligned motion field $\boldsymbol{u}_1(x)$, the LCM $\boldsymbol{m}_1$ of subject 1 can be presented as the motion of boundary control point, $\boldsymbol{m}_1=\boldsymbol{u}_1\left(\boldsymbol{l}_{1,\mathrm{CT}}\right)\epsilon\mathbb{R}^{k\times1}$. Therefore, the LCM repository $\boldsymbol{M}\epsilon\mathbb{R}^{k\times n}$ is reconstructed as,

$$\boldsymbol{M}=[\boldsymbol{m}_1,\boldsymbol{m}_2,\ldots,\boldsymbol{m}_n]=\begin{bmatrix}\boldsymbol{u}_1\left(\boldsymbol{l}_{1,\mathrm{CT},1}\right) & \ldots & \boldsymbol{u}_n\left(\boldsymbol{l}_{n,\mathrm{CT},1}\right)\\ \vdots & \ddots & \vdots\\ \boldsymbol{u}_1\left(\boldsymbol{l}_{1,\mathrm{CT},k}\right) & \ldots & \boldsymbol{u}_n\left(\boldsymbol{l}_{n,\mathrm{CT},k}\right)\end{bmatrix}. \tag{2}$$

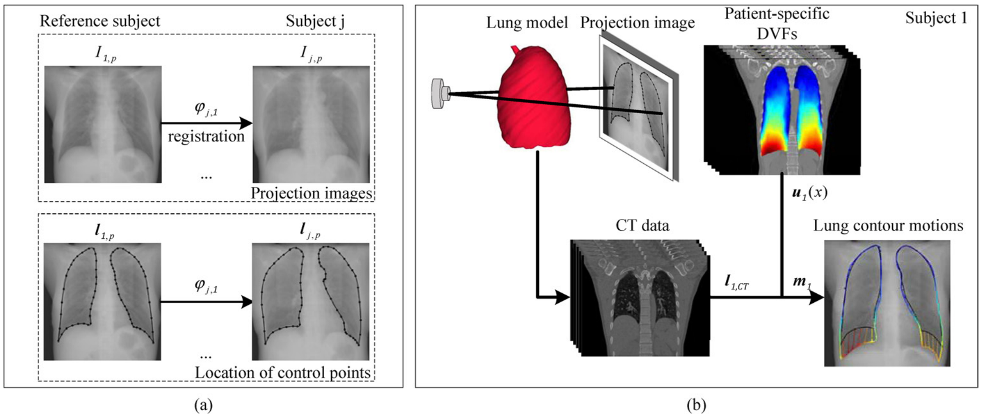

(a) (b)

Figure 2. Overview of the construction of the LCM repository. (a) A transformation $\varphi_{j,1}$ is generated by registering the projection image of subject 1 to the projection image of subject j, and the location of corresponding control points $\boldsymbol{l}_{j,p}$ can be presented as $\boldsymbol{l}_{j,p} = \varphi_{j,1}(\boldsymbol{l}_{1,p})$. (b) The LCM of subject 1 is determined by computing the boundary control point motion from the patient-specific aligned entire lung motion field.

2.3. Sparse respiratory motion representation for the lung

In this study, we aim to estimate the lung respiratory motion based on a set of existing DVFs and LCMs. The basic statistical motion model formulation can approximately present the respiratory motion field $\boldsymbol{u}_i(x)$ of any newly-input patient by a weighed linear combination of lung motion repository $\boldsymbol{u}(x)$.

$$\underset{\boldsymbol{\mu}}{\operatorname{argmin}} \ \|\boldsymbol{u}_i(x) - \boldsymbol{u}(x)\boldsymbol{\mu}\|_2^2, \tag{3}$$

where $\boldsymbol{\mu} = [\mu_1, \mu_2, \ldots, \mu_n]^T$ denotes the linear coefficients of the training samples. Notice that the entire lung motion information cannot be directly acquired from the x-ray image. We analyze the motion of the lung contour between the x-ray image and the projection image to indirectly present the DVF of the newly-input subject. Here, the problem is reformulated as:

$$\underset{\boldsymbol{\mu}}{\operatorname{argmin}} \ \|\boldsymbol{y}_i - \boldsymbol{M}\boldsymbol{\mu}\|_2^2, \tag{4}$$

where $\boldsymbol{y}_{\mathrm{i}}$ is the motion of the newly-input lung contour. We perform the registration between the projection image $I_{i,p}$ of the newly-input CT images $I_{i,\mathrm{CT}}$ and the reference projection image $I_{1,p}$ of subject 1 in the training date set to compute the transformation $\varphi_{i,1}$, such that $I_{i,p} = P \cdot I_{i,\mathrm{CT}} = \varphi_{i,1}(I_{1,p})$, where P is a projection matrix which computes the projection image $I_{i,p}$ from the CT images $I_{i,\mathrm{CT}}$ of the patient at EE breathing phase. Thus, the locations of corresponding control points in the newly-input images can be presented as $\boldsymbol{l}_{i,p} = \varphi_{i,1}(\boldsymbol{l}_{1,p})$. Therefore, equation (4) is rewritten as:

$$\underset{\boldsymbol{\mu}}{\operatorname{argmin}} \ \left\|f_{\mathrm{e}}(f_{\mathrm{ASM}}\left(I_{i,\text{x-ray}}\right), \boldsymbol{l}_{i,p} + \boldsymbol{M}\boldsymbol{\mu})\right\|_2^2, \tag{5}$$

where $I_{i,\text{x-ray}}$ is the x-ray image of the newly-input patient along the LR or AP direction at EI phase. We denote the lung contour in $I_{i,\text{x-ray}}$, determined by ASM, as $f_{\mathrm{ASM}}\left(I_{i,\text{x-ray}}\right)$. f_{e} as the similarity energy which measures the distance between the current locations of control points and the nearest neighbor position on $f_{\mathrm{ASM}}\left(I_{i,\text{x-ray}}\right)$ along the contour normal in the warped lung contour. The displacement of the lung contour in the projection image is driven by the linear combinations $\boldsymbol{M\mu}$ of control point motions in the repository. The problem of the lung contour respiratory motion is converted into a minimization problem of finding the similar LCM of the projection image from contour motion repository to match the lung contour in the x-ray image.

When the number of DVFs in the repository is larger than the number of control points, a unique solution of the statistical motion formulation (equation (5)) may not be guaranteed. Taking into account the determination error in the projection image caused by the ASM method, we explicitly model this error as a sparse vector $\boldsymbol{e}$. Therefore, the optimization problem is reformulated as:

$$\underset{\boldsymbol{\mu}}{\operatorname{argmin}} \left\|f_{\mathrm{e}}(f_{\mathrm{ASM}}\left(I_{i,\text{x-ray}}\right), \boldsymbol{l}_{i,p} + \boldsymbol{M\mu} - \boldsymbol{e})\right\|_2^2 + \lambda_1\|\boldsymbol{\mu}\|_1 + \lambda_2\|\boldsymbol{e}\|_1, \tag{6}$$

where λ_1 and λ_2 are the pre-defined sparsity numbers which control sparseness of $\boldsymbol{\mu}$ and $\boldsymbol{e}$. The LCM can be approximately represented by an optimized sparse linear combination of $\boldsymbol{M\mu} - \boldsymbol{e}$. The $L-1$-norm optimization problem is solved using the homotopy-based method (Asif and Romberg 2014), which has a wide application in face recognition and image reconstruction.

Equation (6) is performed twice as shown in figure 1. In the first iteration, the *L*–*R* x-ray image is used as $I_{i,\text{x-ray}}$ in equation (6). Therefore, the sub-DVFs and the sub-contour motions are reconstructed from the DVF and the contour motions repository in order to decrease the influence of breathing patterns which are not related to the current subject. However, the lung contour respiratory motion along the SI and LR directions cannot be accurately preserved due to the overlapping portion of the lung in the projection image. Hence, the second iteration is employed to represent the motion long these two directions based on the x-ray image in the AP direction. Hence, the sub-DVFs repository, which contains the most similar breathing pattern, is isolated from the whole repository and the newly-input DVF of the entire lung is approximately reconstructed as: $\boldsymbol{u}_i(x) = \boldsymbol{u}(x) \cdot \boldsymbol{\mu}$.

2.4. Optimal adjustment of sparse weight coefficients

We have obtained an approximate respiratory motion model by reconstructing the LCM from the contour motion repository. However, the respiratory motion detail in the entire lung is ignored in the above model. In this section, we optimize the weight coefficients $\boldsymbol{\mu}$ based on the image similarity measure in the area of overlap between the projection image and the x-ray image, such that the projection of the respiratory motion model in the AP direction best matches with the x-ray image in the same direction,

$$\underset{\boldsymbol{\mu}}{\operatorname{argmax}}\ \mathrm{Sim}\left\|I_{i,\text{x-ray}}(x) - P \cdot I_{i,\mathrm{CT}}\left(x + \boldsymbol{u}(x) \cdot \boldsymbol{\mu}\right)\right\|_2^2, \tag{7}$$

where x is the voxel location, $\boldsymbol{u}(x) \cdot \boldsymbol{\mu}$ is the reconstructed motion field of the corresponding voxel reconstructed by the sparse weight coefficient $\boldsymbol{\mu}$, and $I_{i,\mathrm{CT}}(x + \boldsymbol{u}(x) \cdot \boldsymbol{\mu})$ is the warped CT images using the motion field. Finally, Sim is the normalized mutual information (NMI) similarity metric, which is not sensitive to variation of intensity levels. Thus, we only need to seek the optimal weight coefficient $\boldsymbol{\mu}'$ based on the gradient descent method with variable one of non-zero weight coefficients and fixed others. Therefore, the final motion field estimation $\boldsymbol{u}_{\mathrm{i}}(x)$ is represented as: $\boldsymbol{u}_i(x) = \boldsymbol{u}(x) \cdot \boldsymbol{\mu}'$.

Table 1. Data set characteristics of ten testing subjects: breathing type, the tidal volume (ml) and the landmark average motion (mm).

		Tidal volume (ml)		Average motion magnitude (standard deviation) (mm)			
Data set	Breath type	Left lung	Right lung	3D-euclidean	AP	SI	LR
Subject 1	Diaphragmatic	181	190	15.1(7.3)	2.3(1.7)	13.9(9.7)	1.3(1.0)
Subject 2	Diaphragmatic	179	188	13.4(6.7)	2.1(1.6)	12.3(7.9)	1.2(1.0)
Subject 3	Diaphragmatic	147	156	11.6(5.3)	1.9(1.8)	10.8(7.0)	0.8(0.8)
Subject 4	Diaphragmatic	139	149	9.9(4.2)	1.7(1.6)	8.8(5.4)	0.8(0.6)
Subject 5	Thoracic	194	210	15.4(7.9)	5.1(4.9)	12.4(7.9)	1.4(1.3)
Subject 6	Thoracic	193	199	15.2(7.5)	5.0(4.5)	12.3(7.1)	1.3(1.3)
Subject 7	Thoracic	181	187	13.4(6.8)	4.7(4.1)	11.8(6.5)	1.1(0.9)
Subject 8	Thoracic	170	179	12.6(6.6)	3.7(2.9)	10.4(5.9)	1.2(1.1)
Subject 9	Thoracic	154	167	10.4(4.7)	3.5(2.8)	9.3(5.5)	0.9(0.8)
Subject 10	Thoracic	149	162	9.7(4.3)	3.6(2.8)	7.7(4.7)	0.8(0.9)

3. Results

3.1. Image data preparation

The lung respiratory motion field repository consisted of 18 healthy subjects. Ten of them were thoracic breathing pattern and others were diaphragmatic type. CT images were acquired at EE and EI breathing phases using a SIEMENS SOMATOM spirit dual slice CT for each subject, respectively. The spatial resolution of the reconstructed CT data set was $0.912 \times 0.912 \times 1.25\,\text{mm}^3$ (a spatial resolution of $512 \times 512 \times 265$ voxels). The acquisition of CT scans has the approval of the ethics committee (certificate number BJXH20160706C01). The coordinate system of CT images of subject 1 at EE breathing phase was chosen as the reference to construct an aligned respiratory DVF repository and a unified LCM repository for projection images. The lung respiratory DVFs were extracted using a multi-resolution registration framework with registration error less than 1.4 mm and the contour motion repository was constructed based on the motion of the boundary control points.

We evaluated the SMFP-based lung statistical respiratory motion model using 10 other subjects, which were not included in the respiratory motion field repository. Each of these ten subjects had two x-ray images at EI phase along the LR and AP direction, respectively. In order to evaluate the motion estimation in the lung tissue, a semi-automatic tool (Murphy *et al* 2011) was used to detect the landmark position in the lungs at different breathing phases. In this study, the average landmark motion magnitude for each subject is the average distance of corresponding landmark between EE and EI, respectively. Table 1 summarizes all ten testing subjects and includes characteristics of the breathing type, the tidal volume and the average and standard deviation of the landmark motion magnitude. The 3D average motion magnitude of ten subjects is 12.7(6.2) mm and the mean tidal volume is 347.5(33.2) ml.

3.2. Evaluation of SMFP-based LCMs

The optimal parameters (λ_1 and λ_2 in equation (6)) were determined offline using a leave-one-out strategy on 18 subjects in the motion field repository. We found the optimal value of one of them to achieve the best estimation result by fixing anther parameter. We found that the best estimation result was computed in our training data when $\lambda_1 = 40$ and $\lambda_2 = 0.2$. The

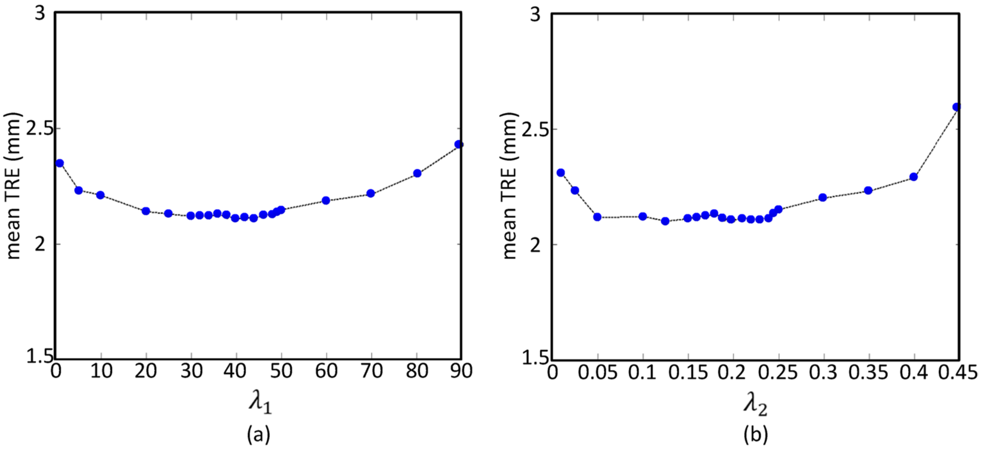

Figure 3. The mean TREs of ten subjects in response to the varied parameters. (a) The TRE curve for different values of λ_1 with $\lambda_2 = 0.2$. (b) The mean TRE curve for different values of λ_2 with $\lambda_1 = 40$.

mean TREs of the ten test subjects in response to varying parameters are shown in figure 3. The motion model used to measure the mean TRE was generated based on two direction projection images. Figure 3(a) shows the mean TRE curve of the respiratory estimation result for different values of λ_1 with $\lambda_2 = 0.2$ and figure 3(b) shows the mean TRE curve for different values of λ_2 with $\lambda_1 = 40$.

The results show that the proposed method has a weak sensitivity to these parameters. Therefore, we used these two values ($\lambda_1 = 40$ and $\lambda_2 = 0.2$) in the following experiments. At first, we compared the LCM estimation result using a single x-ray image along the LR direction with the result using two x-ray images along the LR and AP directions. We used the projection of CT images at EI phase as the ground truth image. The projection image of the original CT images at EE phase, the projection image of reconstructed volumetric images using a single x-ray image, and the projection image of reconstructed volumetric images using x-ray images along the LR and AP directions were compared with the ground truth image respectively. The visual absolute difference comparison of subject 1 in the sagittal and coronal views are shown in figure 4, and the quantitative result is listed in table 3. Since the motion information in the SI direction is not accurately presented in the LR-direction x-ray image, the motion estimation on the sagittal view was poor using the single LR-direction x-ray image, especially on the bottom of the lung (as shown in the second column). The lung contour respiratory motion along the SI and LR directions cannot be accurately preserved due to the overlapping portion of the lung in the projection image. In contrast, the estimation result with two orthogonal x-ray images performed well both on the coronal and sagittal views (as shown in the third column). Lung profiles in the EE image and EI image, the predicted lung profile using the single LR-direction image, and the result using two images are shown in the last column by the yellow, red, green and blue curve, respectively.

The proposed method has been used to estimate the LCM from EE phase to the EI status as shown in figure 5. Each row shows one subject. The ground truth result (red curve) that was segmented manually and the ASM result (blue curve) at EE and EI phase are shown in the first two columns of figure 5. As shown in the second column, we can see that the initial boundary control point detected by ASM has some error. For this reason, we performed a registration between the newly-input images and the reference images to generate corresponding

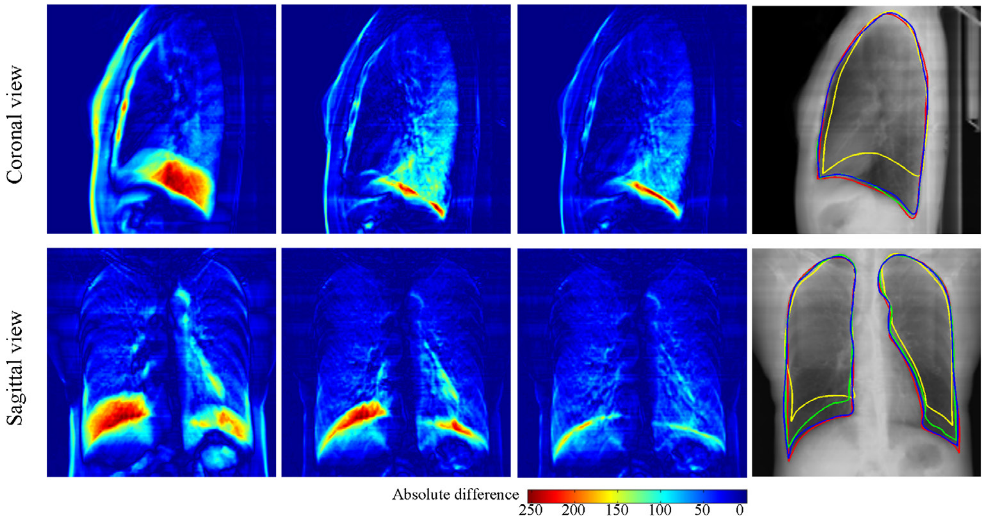

Figure 4. The absolute difference images. (First column) The difference between the ground truth image and the projection image of original CT images at EE phase. (Second column) The difference between the ground truth image and the reconstructed volumetric images using a single x-ray image. (Third column) The difference between the ground truth image and the reconstructed volumetric images using x-ray images along the LR and AP directions. (Fourth column) The shift of the lung profile.

boundary points in the newly-input subject as described in section 2.3. By employing the ASM-based lung contour at EI phase as the target curve, the sparse contour motion estimation (blue curve) using equation (5) fails to match the ground truth lung contour. The result is presented in the third column. In the last column, a better result is achieved based on equation (6) with the $\boldsymbol{e}$ item. We employed the dice similarity coefficient (DSC) to measure the similarity between the ground truth contour and the predicted contour. Given two regions surrounded by the ground truth contour and the predicted contour are regarded as A and B, respectively, the DSC is calculated as $\frac{2|A \cap B|}{|A|+|B|}$. The results are listed in table 2. The mean DSC for all subjects is 89.6(1.9) for the SMFP without $\boldsymbol{e}$ term and 97.5(0.9) for the SMFP with $\boldsymbol{e}$ term.

3.3. Evaluation of SMFP-based lung respiratory motion model

In this section, we compared the spatial motion estimation of the proposed SMFP-based modeling with the PCA method with two principle components. The process of optimizing PCA coefficients was following the method proposed in Li *et al* (2011). In order to qualitatively visualize the deformation field, the motion field achieved by the registration method was regarded as the ground truth. All the experiments were performed on an Intel Xeon quad-core 2.0 GHz processor with 10 RAM, with MATLAB 2014a. The average computation time was 138 s and 125 s for the SMFP method and the PCA method with two principle components, respectively. Figure 6 shows visual comparisons of respiratory DVFs of subject 1–3 between the ground truth and the reconstructed DVFs generated by the PCA method and the proposed method, respectively. The estimation result can be quantified by the target registration error (TRE) of landmarks in table 3. We can see that the maximal motion magnitude occurs at the bottom of the lungs and the deformation magnitude decreases from the bottom to the top of the lungs on the coronal view. In the most lung region, both the PCA and the SMFP method

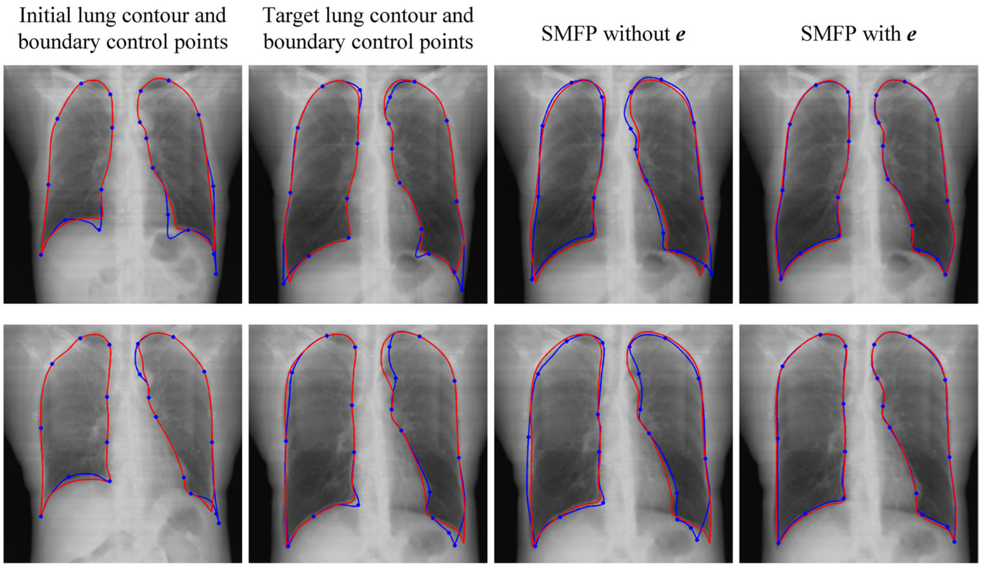

Figure 5. Visual comparison of contour motion estimation results for two subjects. The initial and the target boundary control points detected by the ASM method (first two columns), the sparse contour motion estimation result computed by equation (4) (third column) and the SMFP result achieved by equation (5) (last column). Red cover denotes the manual segmentation result of the lung contours and the blue curves are the estimation results.

Table 2. Quantitative comparisons of contour motion estimation results with and without $\boldsymbol{e}$ term.

	Data set									
Method	1	2	3	4	5	6	7	8	9	10
SMFP without $\boldsymbol{e}$	91	90	92	88	89	90	85	91	87	93
SMFP with $\boldsymbol{e}$	98	97	99	96	98	99	96	97	97	98

achieved an accurate result. While the PCA-based DVF lost some local respiratory motion details (circled regions in figure 6), the SMFP method accurately presented the respiratory DVF. The shortest Euclidean surface distance of the lung surface and the lung vessel tree was measured in the visualization of estimation errors and represented in color (see figure 7). The result of figure 7 is quantitatively evaluated by the average symmetric surface distance (ASSD) value in table 3. Notice the SMFP respiratory motion model has less error compared with the PCA-based model.

A TRE metric is employed to quantitatively evaluate the respiratory motion estimation for all subjects.

$$\mathrm{TRE} = \frac{1}{n}\sum_{i=1}^{n}\left|\boldsymbol{p}_{i,\mathrm{EI}} - \left(\boldsymbol{p}_{i,\mathrm{EE}} + \boldsymbol{u}_i\left(\boldsymbol{p}_{i,\mathrm{EE}}\right)\right)\right|, \tag{8}$$

where n is the number of landmark points, $\boldsymbol{p}_{i,\mathrm{EI}}$ and $\boldsymbol{p}_{i,\mathrm{EE}}$ are the landmark position in EI images and EE images, respectively. $\boldsymbol{u}_i$ is the reconstructed motion field. The ASSD metric is employed to measure the similarity between the lung surface and the lung vessel tree model

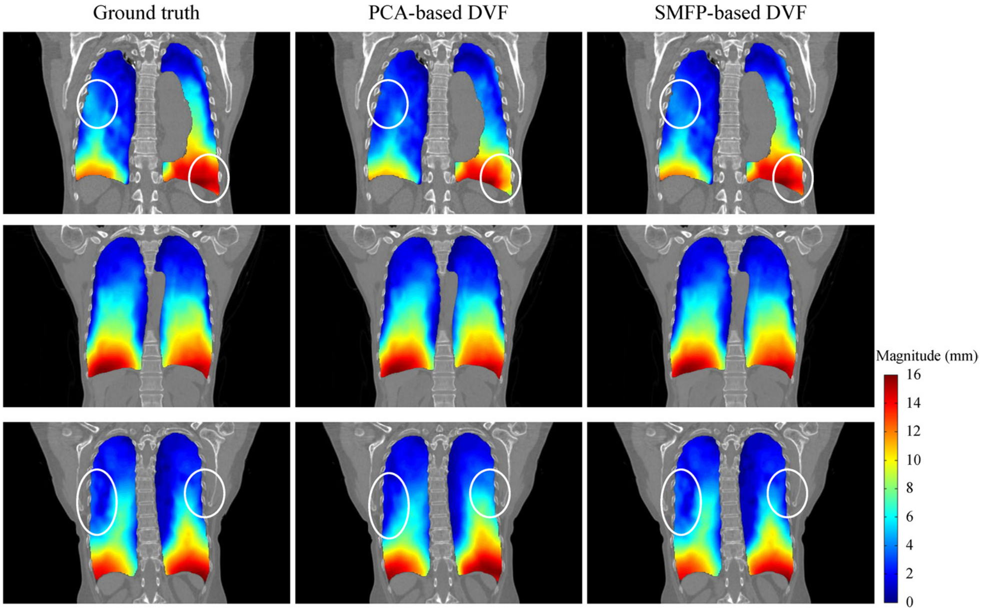

Figure 6. Visualization of computed intra-subject respiratory deformation vector field of subjects 1–3 is shown from the top row to the bottom row between EE and EI phase. From the left to right column are the ground truth result achieved by the registration method, the PCA-based and the SMFP-based respiratory motion estimation results, respectively.

achieved by the reconstructed motion field to the corresponding ground truth models that were segmented by MIMICS (Version 10.01) at the EI phase. The formulation of ASSD is shown below,

$$\mathrm{ASSD}\,(g,e)=\frac{1}{|\boldsymbol{S}(g)|+|\boldsymbol{S}(e)|}\left(\sum_{S_g\in\boldsymbol{S}(g)}d\,(S_g,\boldsymbol{S}(e))+\sum_{S_e\in\boldsymbol{S}(e)}d\,(S_e,\boldsymbol{S}(g))\right),\tag{9}$$

where $\boldsymbol{S}(g)$ and $\boldsymbol{S}(e)$ denote the positions of surface vertices on the ground truth surface model and the estimated surface model, respectively. S_g and S_e are the arbitrary vertex on surface $\boldsymbol{S}(g)$ and $\boldsymbol{S}(e)$ and $d\,(S_g,\boldsymbol{S}(e))$ denotes the shortest Euclidean distance of S_g to the surface $\boldsymbol{S}(e)$. The average and standard deviation of the TRE and ASSD for data sets 1–10 are listed in the table 3.

In table 3, the mean TREs for the PCA-based model, the SMFP-based estimation result with a single LR-direction x-ray image, and the result with two direction x-ray are: 2.5(1.5) mm, 2.4(1.3) mm and 2.3(1.2) mm, respectively. In addition, the ASSD are 2.2(1.5) mm, 2.1(1.4) mm and 2.0(1.1) mm, respectively. We also measured the TRE to evaluate the performance of the optimal adjustment presented in section 2.4 (see table 4). The mean TRE of the SMFP-based model with and without an optimal adjustment for all subjects is 2.3(1.2) mm and 2.5(1.4) mm, repectively.

Table 3. The TRE (mm) of landmark pairs and the ASSD (mm) between the ground truth surface model and the estimated surface model.

		TRE (mm)				ASSD (mm)			
Data set	Method	3D-euclidean	AP	SI	LR	3D-euclidean	AP	SI	LR
1	PCA	3.1(1.4)	1.5(1.4)	2.1(1.9)	1.4(1.4)	2.5(1.4)	1.3(1.0)	1.7(1.2)	0.9(0.8)
	M1[a]	3.1(1.3)	1.4(1.2)	2.1(1.8)	1.0(1.0)	2.4(1.4)	1.3(0.9)	1.7(1.1)	0.7(0.8)
	M2[b]	2.9(1.2)	1.3(1.2)	1.9(1.7)	0.9(0.8)	2.3(1.3)	1.3(0.9)	1.6(1.1)	0.7(0.7)
2	PCA	2.8(1.3)	1.1(1.0)	1.7(1.4)	1.2(0.8)	2.4(1.2)	1.1(0.9)	1.6(1.1)	1.2(0.8)
	M1[a]	2.7(1.2)	1.1(0.9)	1.7(1.3)	1.2(0.8)	2.2(1.3)	1.0(0.8)	1.5(1.2)	1.0(0.9)
	M2[b]	2.4(1.3)	1.1(1.0)	1.6(1.2)	1.1(0.8)	2.1(1.1)	0.9(0.7)	1.4(1.0)	1.0(0.8)
3	PCA	2.3(1.3)	1.1(0.9)	1.8(1.1)	1.2(0.9)	1.9(1.7)	1.0(0.6)	1.3(1.5)	1.1(1.3)
	M1[a]	2.3(1.1)	1.0(0.8)	1.8(1.2)	1.1(0.8)	1.8(1.6)	0.9(0.9)	1.2(1.4)	0.8(0.9)
	M2[b]	2.4(1.3)	1.1(1.0)	1.7(1.0)	1.1(0.5)	1.8(1.4)	0.9(0.8)	0.8(1.3)	0.7(0.8)
4	PCA	2.1(1.7)	1.3(0.6)	1.4(1.3)	1.1(1.3)	2.0(1.8)	1.1(1.0)	1.0(1.5)	1.2(0.7)
	M1[a]	2.0(1.4)	1.1(0.7)	1.4(1.2)	1.1(1.1)	1.9(1.5)	1.0(0.8)	0.9(1.3)	1.2(0.8)
	M2[b]	1.9(1.2)	0.8(0.5)	1.3(1.1)	1.0(1.1)	1.8(1.1)	1.0(0.6)	0.7(1.0)	1.2(0.7)
5	PCA	3.1(2.0)	1.3(1.5)	2.3(1.9)	1.4(1.3)	2.5(1.6)	1.3(1.2)	1.9(1.4)	1.4(1.1)
	M1[a]	3.1(1.8)	1.2(1.3)	2.3(1.5)	1.3(1.2)	2.4(1.5)	1.2(0.9)	1.6(0.9)	1.4(0.9)
	M2[b]	2.9(1.6)	1.1(1.2)	2.2(1.4)	1.2(1.1)	2.4(1.3)	1.1(0.7)	1.3(0.6)	1.4(0.8)
6	PCA	2.8(1.9)	1.2(1.4)	1.8(1.5)	1.2(0.8)	2.3(1.5)	0.9(0.9)	1.8(0.9)	1.5(0.8)
	M1[a]	2.8(1.6)	1.1(1.2)	1.8(1.3)	1.3(0.9)	2.2(1.3)	0.8(0.6)	1.9(0.8)	1.4(0.7)
	M2[b]	2.7(1.2)	1.0(0.9)	1.7(1.0)	1.2(0.8)	2.2(0.9)	0.7(0.5)	1.8(0.8)	1.3(0.6)
7	PCA	2.7(1.5)	1.2(1.1)	1.8(1.3)	1.2(0.9)	2.3(1.2)	1.0(0.8)	1.4(1.1)	1.4(0.6)
	M1[a]	2.6(1.5)	1.1(1.0)	1.8(1.3)	1.2(0.8)	2.2(1.1)	0.9(0.7)	1.4(1.0)	1.3(0.5)
	M2[b]	2.5(1.2)	1.0(0.9)	1.8(1.1)	1.1(0.8)	2.1(0.9)	0.9(0.6)	1.3(0.8)	1.3(0.3)
8	PCA	2.4(1.2)	1.0(0.7)	1.6(1.1)	1.2(0.8)	2.2(1.4)	1.2(0.7)	1.3(1.1)	1.1(0.9)
	M1[a]	2.3(1.2)	0.9(0.8)	1.6(1.2)	1.1(0.7)	2.3(1.6)	1.2(0.8)	1.4(1.1)	1.2(1.0)
	M2[b]	2.3(1.0)	0.9(0.8)	1.4(0.9)	1.0(0.7)	2.2(1.5)	1.1(0.8)	1.4(1.0)	1.2(0.9)
9	PCA	2.0(0.9)	0.8(0.5)	1.2(0.8)	1.1(0.5)	2.1(1.7)	1.4(0.8)	1.8(1.2)	0.9(0.8)
	M1[a]	1.9(0.9)	0.7(0.6)	1.2(0.8)	1.0(0.5)	2.0(1.5)	1.2(0.7)	1.6(1.1)	0.9(0.7)
	M2[b]	1.9(0.8)	0.7(0.6)	1.2(0.7)	0.9(0.4)	1.8(1.0)	0.9(0.4)	1.5(0.9)	0.8(0.6)
10	PCA	1.8(1.3)	1.0(0.9)	1.1(1.1)	0.8(0.4)	1.9(1.4)	0.7(0.9)	1.0(1.3)	0.9(0.9)
	M1[a]	1.7(1.2)	0.9(0.8)	1.1(0.9)	0.8(0.4)	1.8(1.1)	0.6(0.8)	1.0(1.0)	0.8(0.7)
	M2[b]	1.6(0.9)	0.8(0.5)	1.0(0.8)	0.8(0.3)	1.7(0.9)	0.6(0.5)	0.9(0.8)	0.7(0.6)

[a] The SMFP-based estimation result with a single LR-direction x-ray image.

[b] The SMFP-based estimation result with two direction x-ray images.

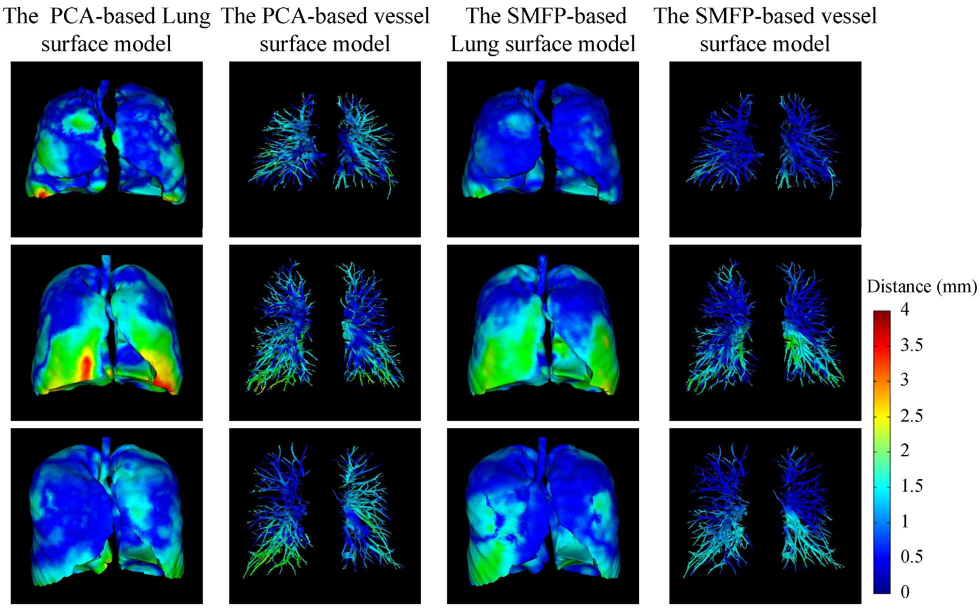

Figure 7. The visualization of estimation errors of the lung surface and lung vessel tree surface of subjects 1–3. The first and second column are the visual error of PCA respiration motion models, while the last two columns are the error of SMFP respiration motion models.

3.4. Evaluation of SMFP-based lung respiratory motion mode for 4DCT data sets

In this section, two 4DCT data sets were acquired from the Léon Bérard Cancer Center & CREATIS lab (Vandemeulebroucke *et al* 2011). The CT scan at EE phase was used as the reference image and the projection of the CT scan at EI phase was used to simulate the newly-input biplane x-ray image. The remaining 4DCT data sets were employed to evaluate the accuracy of the motion model. The mean landmark motion (blue line) and the mean TRE of the SMFP-based model (red line) are shown figure 8.

4. Discussion

In order to preserve respiratory motion detail and reduce the treatment cost for patients in lung image-guided interventions, we presented a novel patient-specific statistical modeling method based on two x-ray images along the LR and AP directions. In the application of lung respiratory motion estimation, ten subjects were used to evaluate the reliability of the proposed modeling method. Our lung motion repository was constructed from 18 healthy subjects and the unified boundary control points on the lung contour at EE breathing phase were employed to extract the LCM from the DVF repository. The sparse weight coefficients of the SMFP-based motion model were determined by equation (6) and fine-tuned based on the similarity between the projection image and the x-ray image along the AP direction, such that the projections of the reconstructed volumetric newly-input images best match the x-ray image in each direction, respectively. Thus, the newly-input lung motion field was approximately represented with a sparse combination of the sub-DVF in the repository.

Table 4. The mean TRE of the motion model with and without the optimal adjustment.

	Data set									
Method	1	2	3	4	5	6	7	8	9	10
SMFP[a]	3.0(1.2)	2.4(1.5)	2.5(1.5)	2.0(1.4)	3.4(1.9)	2.7(1.1)	2.7(1.3)	2.2(1.3)	1.9(0.8)	1.8(1.5)
SMFP[b]	2.9(1.2)	2.4(1.3)	2.4(1.3)	1.9(1.2)	2.9(1.6)	2.7(1.2)	2.5(1.2)	2.3(1.0)	1.9(0.8)	1.6(0.9)

[a] The SMFP-based model without an optimal adjustment.

[b] The SMFP-based model with an optimal adjustment.

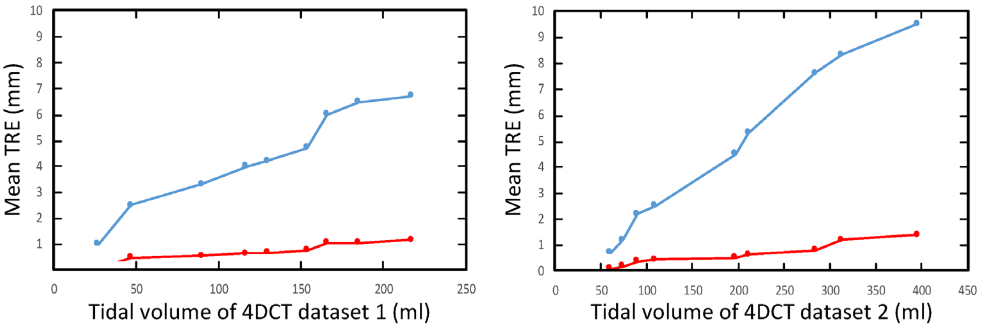

Figure 8. The mean TRE of the SMFP-based lung respiratory motion mode for 4DCT data sets. The mean landmark motion and the mean TRE of the SMFP-based model are denoted by blue and red lines, respectively.

As shown in figure 3, the respiratory motion estimation of ten subjects are stable in a wide range value of λ_1 and λ_2 and the mean TRE for ten subjects is ranged from 2.1 to 2.4 mm, and 2.1 to 2.6 mm for different values of λ_1 and λ_2, respectively. If the value of λ_2 is extremely large, we achieved relatively larger mean TRE due to $\boldsymbol{e}$ in equation (6) approximating zero. Thus, the LCM estimation result is similar with the third column of figure 5. We can see that the deformed LCM estimation using equation (6) performs a reasonable estimation result in contrast to the result using equation (5) as shown in last two columns of figure 5 and table 2. The reason is that the target lung contour detected by the ASM method, which was regarded as the target curve $f_{\text{ASM}}\left(I_{i,\text{x-ray}}\right)$ in equation (5), had some errors (the second column of figure 5). In contrast, the deformed lung contour driven by these linear combinations $\boldsymbol{M\mu}-\boldsymbol{e}$ successfully generated a reasonable lung contour due to the L1 norm constrain of $\boldsymbol{e}$**,** which handles the missing lung contour detection.

The LCM results of testing subject 1 with and without second x-ray image along the AP direction were shown in figure 4 on the sagittal and coronal views. The predicted contour, only using the LR direction x-ray image, failed to match the bottom of the lung contour at EI phase on the coronal view. The reasons are threefold: First, our lung motion repository consisted of different breathing patterns which lead to some regions preserving the same 3D-Euclidean motion magnitude with the different motion in the AP and SI directions as shown subjects 2 and 7 in table 1. Second, the motion information in the SI direction was not preserved clearly using a single LR-direction x-ray image due to the overlap of the left lung and the right lung in this orientation. Similarly, the influence of the lung tissue overlaps existed by using a single other direction (AP direction) x-ray image. Third, the motion detail in the LR direction was also lost in the x-ray image along the LR direction. In contrast, the estimation result by adding the x-ray image along the AP direction in the optimization process achieved a relative ideal shape match on the two views.

Finally, the full motion detail in the entire lung may be ignored in the motion model derived from the surface, due to the similar breathing pattern which may contain the same respiratory motion of the lung surface and the different motion detail of the lung tissue. Therefore, the optimal sparse weight coefficients $\boldsymbol{\mu}'$ were obtained based on the image similarity measure in the area of overlap between these two images, such that the projection of our respiratory motion model driven CT images in the AP direction best matches with the x-ray image in the same direction. Table 4 shows that most of the SMFP-based motion model achieved a more accurate prediction result by employing the optimal adjustment.

We compared the SMFP-based method with the PCA method. Both of them achieve a comparable result, while the SMFP-base motion field preserves more accurate local motion information (as seen in circled regions in figure 6) than the PCA based motion field. The shortest Euclidean surface distance of the lung surface and the lung vessel tree is measured in the visualization of estimation errors in figure 7. The estimation error on the SMPF-based surface model also shows a more accurate estimation than the PCA-based model. The average motion prediction error (TRE) of the landmark pairs achieved by the SMFP method with two directions x-ray images and the PCA method ranged from 1.6(0.9) to 2.9(1.6) mm and 1.8(1.3) to 3.1(2.0) mm, respectively. The similarity between the ground truth surface model and the surface model achieved by the reconstructed motion field based on the two modeling methods was measured by the ASSD metric. It can be seen that the SMFP-based surface model is a more accurate match to the ground truth model than the PCA-based model, which only preserved the principal components of the respiratory motion information and discarded some local motion details. Even though the PCA model can also preserve the motion detail by using all the PCA eigenvectors and coefficients, it may lead to overfitting and larger errors (Li *et al* 2011). The results show that the average percentage improvements of our approach to the PCA-based model are 6.5% for TRE and 7.8% for ASSD. What's more, the estimation result using a single LR-direction x-ray image has a poor performance compared with the result using two x-ray images as shown in table 3. The implementation on MATLAB 2014a of the proposed method takes around 138 s, while 125 s in average for the PCA method, which shows that the SMFP method not only successfully preserves motion detail but also performs a high efficiency of calculation by using the homotopy-based method.

In previous literatures, the mean TRE obtained based on the PCA method was usually less than 2 mm. While the largest TRE is 3.1(2.0) mm in our study. There are many possible reasons for the difference in TRE. Firstly, in previous works, the PCA based model is constructed based on 4DCT data sets for each patient, while our PCA based model was formulated based on only two CT scans (EE and EI phase). Secondly, the TRE usually increases with increasing motion magnitude of the landmark (see figure 8). For instance, the average motion magnitude was 11.2 mm and the obtained TRE was 2.1(0.3) mm in the study of Li *et al* (2011). The similar testing subject in our study is Subject 3 (11.6 mm for the motion magnitude) and a similar value of the TRE is obtained, TRE = 2.3(1.3) mm. Thirdly, different image resolutions, registration methods, landmark detection methods and landmark locations also lead to a variation of the TRE. In this study, we followed the optimization method proposed by Li *et al* to optimize PCA coefficients (Li *et al* 2011) and we did not make any further improvement to the PCA method. Currently, the error term in the SMFP method is not suitable for application to the PCA method. The main reason is that the error term is used to handle the missing lung contour detection. In contrast, the PCA method does not employ the LCM to optimize coefficients in the existing modeling method.

In this study, volunteers were asked to take a deep breathing to ensure CT image pairs approximately obtained at the proper EE and EI phases, which are used to construct the lung motion repository. However, this monitoring technique cannot ensure the CT images pairs are obtained at the proper EE and EI phases. This uncertainty may influence the respiratory motion amplitude, but the motion tendency has been preserved in the DVFs. To deal with this problem, both equations (6) and (7) are employed to ensure the newly-input motion field can be approximately presented by a sparse linear combination of the sub-DVFs and the respiratory motion amplitude of these sub-DVFs also can be modified by tuning the sparse coefficient $\boldsymbol{\mu}$. Moreover, the experiment result shows that the proposed framework achieved a comparable estimation result. As shown in figure 1, it is unnecessary to repeatedly obtain the EE and EI images to generate the motion field of the newly-input patient by using the proposed modeling method. Following the biopsy process presented in our previous study (Chen *et al* 2017), a reference needle is positioned in the region near the ROI before the operation. The motion estimation error of the ROI can be handled by the motion of the electromagnetic tracked reference needle in the future biopsy clinical experiment.

The proposed method can be employed to generate a series of lung motion models for different phases by using the projection of the first 4DCT scan at EE phase as the reference image, and the projection images of the later 4DCT scans as the target images, respectively. However, the patient scan times will increase for acquisition of biplane x-ray images at different breathing phases to generate the approximated continuous to response to the hysteresis phenomena. The motion model presented in this study is planned to guide the percutaneous biopsy in the future. In order to reduce the dose for the patient and the surgeon during the biopsy, a BEM motion modeling method based on two CT scans acquired from EE and EI phases was proposed in our previous work (Chen *et al* 2017). We employed two needles (a reference and a biopsy needle) to perform a peripheral biopsy. The reference needle is positioned in the region near the lesion before the biopsy operation based on the experience of a thoracic surgeon. The motion of the reference needle achieved by a magnetic tracker is used to derive the motion model to compute the location of the lesion. Since the reference needle is close to the lesion, the hysteresis phenomena of the target region can be approximately represented by the motion of this reference needle tip. Following the idea of our previous study, the motion of the tissue can be predicted by employing the SMFP based motion model instead of the BEM model.

5. Conclusion

In this study, we presented a novel statistical respiration motion modeling method based on two x-ray images along the LR and AP directions. We employed these two x-ray images to extract the motion information using ASM and combined the motion of boundary control points with the LCM repository to optimize the sparse weight coefficients. The coefficients were fine-tuned based on the similarity between the projection image of the reconstructed volumetric images and the x-ray image along the AP direction. Therefore, the lung respiratory motion field was approximately reconstructed by these weight coefficients with the corresponding DVF in the respiratory motion repository. The proposed method was successfully applied to 10 subjects and achieved a competitive estimation result. The main contribution of this proposed method is to effectively preserve the respiratory local motion information. In addition, we integrated the LCMs to the statistical motion model with two x-ray images and solved the difficulties of entire lung estimation by optimizing the sparse weight coefficient.

The influence of noise, scatter and other physical effects may indeed degrade the quality of the projection images and lead to the prediction inaccuracy. We will investigate methods for creating the projection image, such as machine learning based techniques, to enhance the robustness of the proposed method with respect to noise in the future. In addition, we look forward to receiving more lung motion samples to meet the requirements of clinical practice, and constructing a compact and informative motion repository using a dictionary learning algorithm, such as K-SVD method. Lastly, we also plan to apply a feasible automatic estimation method for parameters of the proposed method.

Acknowledgment

This research is partially supported by the National Key research and development program (2016YFC0106200) and 863 national research fund (2015AA043203) as well as the Chinese NSFC research fund (61190120, 61190124 and 61271318).

ORCID iDs

Lixu Gu https://orcid.org/0000-0002-6210-4847

References

Asif M S and Romberg J 2014 Sparse recovery of streaming signals using l_1 -homotopy *IEEE Trans. Signal Process.* **62** 4209–23

Chen D, Chen W, Huang L, Feng X, Peters T and Gu L 2017 BEM-based simulation of lung respiratory deformation for CT-guided biopsy *Int. J. Comput. Assist. Radiol. Surg.* **12** 1585–97

Cootes T F, Taylor C J, Cooper D H and Graham J 1995 Active shape models-their training and application *Comput. Vis. Image Underst.* **61** 38–59

Ehrhardt J, Werner R, Säring D, Frenzel T, Lu W, Low D and Handels H 2007 An optical flow based method for improved reconstruction of 4D CT data sets acquired during free breathing *Med. Phys.* **34** 711–21

Ehrhardt J, Werner R, Schmidt-Richberg A and Handels H 2011 Statistical modeling of 4D respiratory lung motion using diffeomorphic image registration *IEEE Trans. Med. Imaging* **30** 251–65

Fuerst B, Mansi T, Carnis F, Sälzle M, Zhang J, Declerck J, Boettger T, Bayouth J, Navab N and Kamen A 2015 Patient-specific biomechanical model for the prediction of lung motion from 4D CT images *IEEE Trans. Med. Imaging* **34** 599–607

Guerrero T, Zhang G, Huang T-C and Lin K-P 2004 Intrathoracic tumour motion estimation from CT imaging using the 3D optical flow method *Phys. Med. Biol.* **49** 4147–61

Heinrich M P, Papiez B W, Schnabel J A and Handels H 2014 Non-parametric discrete registration with convex optimisation *Proc. Biomedical Image Registration: 6th Int. Workshop, WBIR 2014 (London, UK, July 7–8, 2014)* **8545** 51–61

King A P, Buerger C, Tsoumpas C, Marsden P K and Schaeffter T 2012 Thoracic respiratory motion estimation from MRI using a statistical model and a 2D image navigator *Med. Image Anal.* **16** 252–64

Li M, Castillo E, Zheng X-L, Luo H-Y, Castillo R, Wu Y and Guerrero T 2013 Modeling lung deformation: a combined deformable image registration method with spatially varying Young's modulus estimates *Med. Phys.* **40** 81902

Li R, Lewis J H, Jia X, Zhao T, Liu W, Wuenschel S, Lamb J, Yang D, Low D A and Jiang S B 2011 On a PCA-based lung motion model *Phys. Med. Biol.* **56** 6009–30

McClelland J R, Hawkes D J, Schaeffter T and King A P 2013 Respiratory motion models: a review *Med. Image Anal.* **17** 19–42

Murphy K, van Ginneken B, Klein S, Staring M, de Hoop B J, Viergever M A and Pluim J P W 2011 Semi-automatic construction of reference standards for evaluation of image registration *Med. Image Anal.* **15** 71–84

Peltz C D, Divine G, Drake A, Ramo N L, Zauel R, Moutzouros V and Bey M J 2015 Associations between *in vivo* glenohumeral joint motion and morphology *J. Biomech.* **48** 3252–7

Preiswerk F, De Luca V, Arnold P, Celicanin Z, Petrusca L, Tanner C, Bieri O, Salomir R and Cattin P C 2014 Model-guided respiratory organ motion prediction of the liver from 2D ultrasound *Med. Image Anal.* **18** 740–51

Vandemeulebroucke J, Rit S, Kybic J, Clarysse P and Sarrut D 2011 Spatiotemporal motion estimation for respiratory-correlated imaging of the lungs *Med. Phys.* **38** 166–78

Weichert F, Wawro M, Müller H and Wilke C 2004 Registration of biplane angiography and intravascular ultrasound for 3D vessel reconstruction *Methods Inf. Medicine* **43** 398–402 (PMID:15472753)

Werner R, Schmidt-Richberg A, Handels H and Ehrhardt J 2014 Estimation of lung motion fields in 4D CT data by variational non-linear intensity-based registration: a comparison and evaluation study *Phys. Med. Biol.* **59** 4247–60

Yang W, Sun W, Li Q, Yao Y, Lv T, Zeng J, Liang W, Zhou X and Song Y 2015 Diagnostic accuracy of CT-guided transthoracic needle biopsy for solitary pulmonary nodules *PLoS One* **10** e0131373

Zhang G, Huang T-C, Guerrero T, Lin K-P, Stevens C, Starkschall G and Forster K 2008 Use of three-dimensional (3D) optical flow method in mapping 3D anatomic structure and tumor contours across four-dimensional computed tomography data *J. Appl. Clin. Med. Phys.* **9** 59–69